Original Article

Institution of MECHANICAL ENGINEERS

Journal of MECHANICAL ENGINEERING SCIENCE

Proc IMechE Part C:
J Mechanical Engineering Science
1–11

DOI: 10.1177/09544062221139968
journals.sagepub.com/home/pic
SAGE

A nine-degree-of-freedom modular redundant robotic manipulator: Development and experimentation

Huayang Sai[1,2], Yanhui Li[1], Shuai He[1], Enyang Zhang[1], Mingchao Zhu[1] and Zhenbang Xu[1]

Abstract

Performing interactive tasks in complex obstacle environments is a formidable challenge for manipulators. Redundant manipulators have the advantage of being highly flexible and can be used to perform interactive tasks in complex environments. This paper presents a nine-degree-of-freedom (DOF) modular redundant manipulator with nine identical modular joints. To improve the obstacle avoidance capability in narrow environments, the bidirectional rapidly-exploring random trees (bi-RRT) algorithm and the oriented bounding box (OBB) are combined for trajectory planning of redundant robotic manipulators. To enhance the interaction capability in uncalibrated dynamic environments, an improved virtual semi-active damping control (VSADC) algorithm based on particle swarm optimization (PSO) is proposed, and it can effectively estimate impedance parameters and positions of the dynamic environment. Finally, combined with the proposed control schemes, simulation and experimental results demonstrate that the designed redundant manipulator can traverse complex obstacle environments and interact with the unknown dynamic environment.

Keywords

Redundant manipulator, modular, obstacle avoiding, semi-active damping

Date received: 11 September 2022; accepted: 2 November 2022

Introduction

Redundant manipulators with high flexibility can complete demanding tasks in the narrow and numerous unstructured workspaces with obstacles, such as on-orbit service,[1] nuclear,[2] and minimally invasive surgery.[3] Since the 1970s, after a redundant tensor manipulator was proposed, it has attracted a significant amount of interest due to its superior performance.[4]

Generally, redundant manipulators can be divided into articulated multi-section structures and continuum structures according to their structural characteristics. The cable-driven redundant manipulators are a typical kind of continuous redundant manipulators, which usually have slender bodies and huge drives,[5] and they are suitable for exploration in narrow environments.[1,6,7] There are other types of continuous manipulators, such as Saab et al.[8] designed a novel space articulated robot, which realizes the movement of the manipulator through gears and braided nylon cables. This type of manipulator usually has a small load capacity and low accuracy. The redundant manipulator of articulated multi-section structures comprises multiple joint units in series and generally has higher control accuracy than the continuous manipulator. An impressive example is the snake robot designed by Carnegie Mellon University, which can cross complex obstacle environments through friction with the environment.[9,10] Mu et al.[11] designed two snake-like robots with spherical joints for environmental exploration. These snake-like robots can be applied in exploring unstructured environments, but they often do not have a large enough load to perform complex interactive tasks. Parallel structure is used extensively in the design of redundant manipulators due to its large load and adjustment accuracy. Gallardo et al.[12] designed a redundant manipulator with parallel mechanism modules as the

[1]CAS Key Laboratory of On-Orbit Manufacturing and Integration for Space Optics System, Changchun Institute of Optics, Fine Mechanics and Physics, Chinese Academy of Sciences, Changchun, Jilin, China
[2]University of Chinese Academy of Sciences, Beijing, China

Corresponding author:
Zhenbang Xu, CAS Key Laboratory of On-Orbit Manufacturing and Integration for Space Optics System, Changchun Institute of Optics, Fine Mechanics and Physics, Chinese Academy of Sciences, No. 3888 Dong Nanhu Road, Changchun, Jilin 130033, China.
Email: xuzhenbang@ciomp.ac.cn

mechanical joint. Similarly, Zhao et al.[13,14] and Hu et al.[15] designed redundant manipulators composed of parallel modules. These manipulators have high positioning accuracy, but the modeling is complex, and the flexibility of the manipulator is inevitably limited due to the large joint volume. Some redundant manipulators are composed of series hinged rigid links, such as the redundant manipulators designed by Brown et al.[16] Nonetheless, even if numerous researches have been done, redundant manipulators with multi-section structures mainly suffer from large size and difficulty in interaction, modeling, and control, which is required to be further investigated.

Although redundant manipulators are suitable for complex and constrained environments, planning a possible path for redundant manipulators and controlling their interaction with the environment is not easy. The trajectory planning of snake-like robots focuses on the obstacle environment of two-dimension (2D),[11] and some trajectory planning methods of redundant manipulators only stay in the simulation due to the complexity of the redundant manipulator.[17–19] Moreover, few results have considered collision detection between joints of redundant manipulators in obstacle avoidance.[20] Therefore, developing efficient trajectory planning algorithms for highly redundant manipulators in obstacle environments remains a significant challenge. In particular, not only numerical simulations but also experiments should be performed to demonstrate the effectiveness of the proposed trajectory planning algorithm.

Moreover, force control of the redundant manipulator is a necessary technology for performing interactive tasks. However, setting controller parameters for actual contact tasks with unknown environments is not an easy task. Especially the environmental position is not calibrated and also the contact position cannot be determined from the force sensor information due to the presence of force measurement thresholds. These existing force control methods mostly assume some prior environmental knowledge,[21,22] and it is difficult to obtain accurate information about the environment in practice. Some impedance methods based on neural networks and iterative learning have been designed to obtain impedance models with better performance, but they rely on large amounts of preprocessed data to train the samples.[23,24] To solve the above problem, an estimation algorithm based on L-BFGS has been proposed in our previous study, but it can only be applied to static environments.[25] Therefore, it is necessary to develop a more powerful impedance control algorithm to face the uncalibrated dynamic environment, which is important for the practical application of the redundant robotic manipulator.

In this paper, a novel modular redundant manipulator is designed, composed of nine consistent joint modules in series. A single joint is compact enough to allow the manipulator to cross a narrow environment and sufficient torque to support the weight of the manipulator itself. Combined with the proposed trajectory planning and force control algorithm, the advantages and future research directions of the designed manipulator is discussed. Specifically, the major contributions of this paper are as follows:

1. A novel modular redundant manipulator is designed and manufactured with a large load capacity and compact structure.
2. Based on the bi-RRT and OBB algorithm, a trajectory planning algorithm for redundant manipulators in 3D obstacle environment is proposed. The proposed trajectory planning algorithm improves the path planning efficiency of traditional RRT, and the effectiveness of the algorithm is verified by system simulation and experiment.
3. Based on iterative mindset, an improved VSADC algorithm is proposed for robotic manipulators to interact with dynamic and unknown environments, which solves the problem that the existing VSADC technique can only be used for static environments.

The remainder of the paper is organized as follows. Section 2 introduces the manipulator and the joint structure. Trajectory planning and the force control algorithm are designed in Section 3 and simulations and experiments are performed in Section 4. In Section 5, we discuss the experimental results and some future work. The conclusions of our work are presented in Section 6.

Mechanical design

Structural design of the redundant manipulator

The 9-DOF modular redundant manipulator mechanical design, shown in Figure 1, consists of nine identical modular joints connected in series. The adjacent joints of the manipulator are connected vertically along the joint center axis (see Figure 1(c)), and the number of joint modules can be expanded and reduced according to the task requirements. Based on the improved Monte Carlo method and voxel algorithm,[26] Figure 1(d) shows the reachable workspace and dexterous workspace of the designed manipulator. Dexterous workspace can be calculated to account for 56.9% of the reachable workspace for the designed redundant manipulator. Therefore, the designed redundant manipulator has more flexibility than general industrial manipulators. The housing structure of the joint is designed to be lightweight to reduce the impact of the mass of the manipulator on the load of the manipulator, and the designed redundant manipulator has enough strength to support itself compared to snake robots. The system

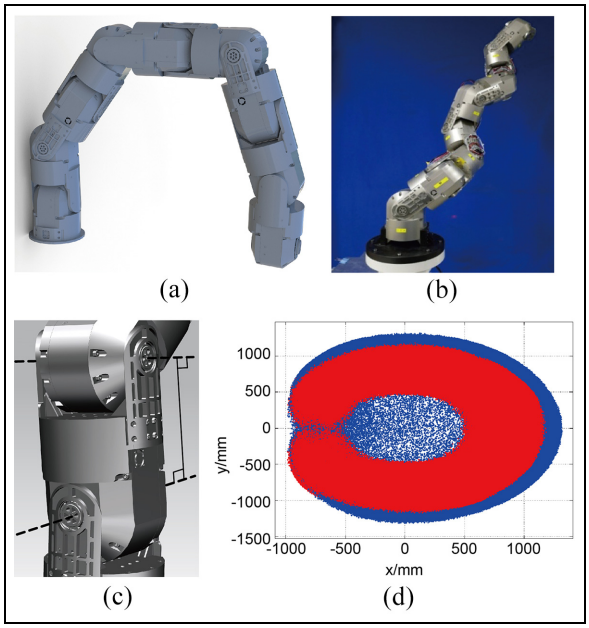

Figure 1. Structure of the redundant manipulator: (a) 3D model of the manipulator, (b) physical diagram of the manipulator, (c) schematic diagram of the connection between the adjacent joints, and (d) reachable workspace and dexterous workspace of the manipulator. The red dots indicate the dexterous workspace, and the blue dots indicate the reachable workspace.

Table 1. Overview of the manipulator system parameters.

Parameter	Quantity
Dimensions	Joint diameter: 69.5 mm Joint length: 166 mm Nine-DOF manipulator: 1.49 m
Mass	Joint mass: 3.42 kg Nine-DOF manipulator: 30.60 kg
Actuation	Max torque: 190 Nm Max speed: 2.83 RPM
Power	Voltage: 24 V Rated power: 630 W
Communication	100 Mbps Ethernet
Sensor	Motor angle and speed sensors Voltage sensors Current sensors
Workspace	9.5576×10^9 mm^3
Joint rotation range	$[-\pi/2, \pi/2]$ rad

parameters of the designed redundant manipulator are shown in Table 1.

Modular joint design

The designed modular joint is shown in Figure 2. It can be seen that the housing structure of the joint mainly consists of three parts: upper housing, middle housing, and lower housing, and each housing is connected by bolts. Two connecting plates are fixed on both sides of the joint end, and they are fixed to the output shaft of the adjacent joint by a rigid connecting shaft. Figure 2(b) and (c) show the arrangement of the internal structures of the modular joint, and a harmonic reducer connects the input and output shafts of the joint. A circular grating ruler is mounted on the output shaft and is used to measure the actual rotation angle of the joint. A spur gear reducer is mounted at the end of the motor and transmits the power to the harmonic reducer with a timing pulley. The electronics, such as the driver, are fixed to the upper part of the motor, and they are used for joint angles, speed, and torque control. The thermal control module is a cooling fan, which is necessary for the manipulator to work for a long time. Compared to the redundant manipulators composed of parallel mechanism modules,[13–15,27] the designed manipulator has a larger length-diameter ratio. Additionally, different from the snake redundant robots,[9–11] the end of the designed manipulator provides a large enough load capacity to perform interactive tasks such as handling.

The designed joint can allow the wire connection between two adjacent joints embedded in the recess of the auxiliary connecting plate, as shown in Figure 2(d). The main connection plate is installed outside the auxiliary connecting plate to avoid the manipulator wiring exposure and entanglement. The designed manipulator requires only one communication bus and power cable to connect to each joint of the manipulator, where the communication bus and power cable are arranged in the connection boards on both sides of the joint. Compared to the redundant manipulator in Xu et al.,[28] the cables of the designed manipulator are not exposed, which outwardly ensures that the manipulator can perform its tasks safely.

Trajectory planning and force control algorithms

Trajectory planning algorithm based on bi-RRT and OBB

The method of RRT was proposed by LaValle and Kuffner[29] to provide a suitable path between previously known start and target positions for a robot with multiple DOFs. To improve the computational efficiency of the RRT algorithm, the advanced version of the RRT is the bi-RRT algorithm, which uses two trees to plan a suitable collision-free path for robotic manipulators.[30] The two trees constructed by the bi-RRT algorithm begin branching from initial and target locations toward each other until the leaves of the two trees overlap. The algorithm stops the search process when any two branches of the trees meet at a specific location. The overlapping leaves can achieve a collision-free path from the initial tree to the target tree.

Among the many collision detection algorithms, the bounding volume hierarchy is one of the most

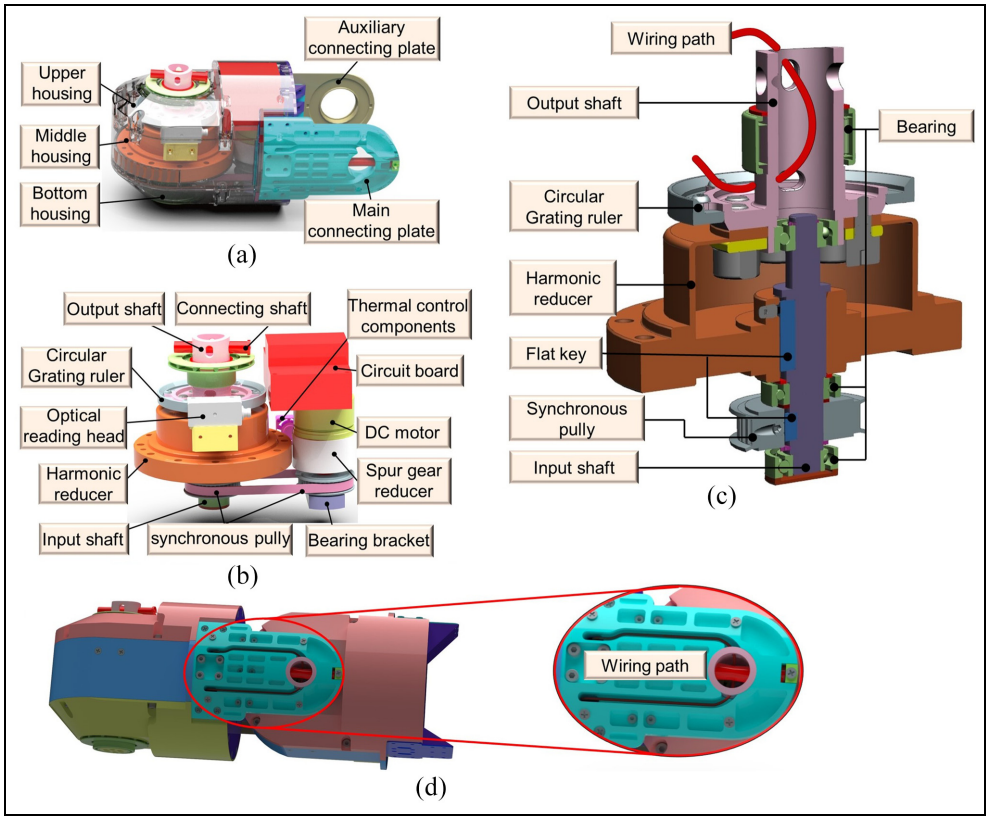

Figure 2. Model diagram of the modular joint: (a) joint assembly diagram, (b) components inside the joint, (c) model diagram of joint output shaft assembly, and (d) model diagram of adjacent joint connection and wiring.

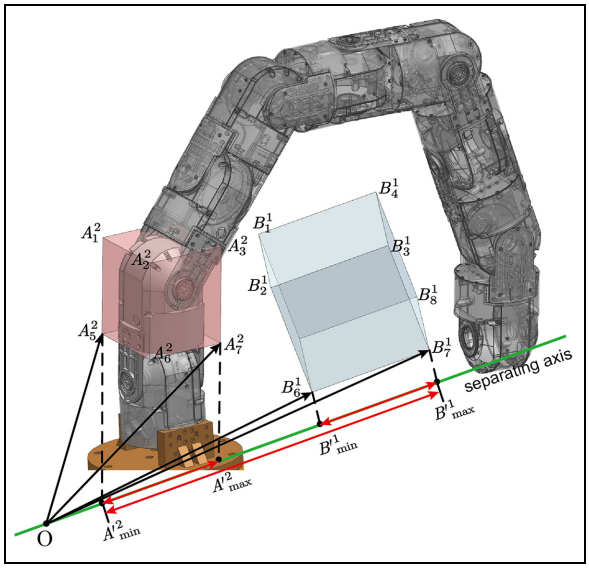

Figure 3. Collision detection of manipulator based on OBB algorithm.

successful in modern systems.[31] In this paper, the OBB algorithm is used to detect whether there is a collision between the manipulator and the obstacle. As shown in Figure 3, rectangles are used to surround modular joints and obstacles, respectively. Define A_{ia}^{n} as the bounding box of the joint $n(n = 1, \cdots, 9)$ and the vertex $ia(ia = 1, \cdots, 8)$, and B_{ib}^{k} represents the vertex $ib(ib = 1, \cdots, 8)$ of the obstacle bounding box k in the workspace. Taking the joint 2 as an example, these two OBBs have 15 potential separating axes, 6 of which are the directional axes of two cuboids, and 9 are the cross-product of the directional axes. In Figure 3, a separation axis is obtained by taking the cross product of the direct axis $\overrightarrow{A_3^2A_7^2}$ and $\overrightarrow{B_8^1B_7^1}$. Then, each vertex of OBB is projected onto the separation axis. If the projection lines of each vertex of two OBBs do not overlap, such as

$$\left|\overrightarrow{A'^2_{\min}A'^2_{\max}}\right| + \left|\overrightarrow{B'^1_{\min}B'^1_{\max}}\right| < \left|\overrightarrow{A'^2_{(i)}B'^1_{(i)}}\right|_{\max}, \quad (1)$$

then it can be considered that joint 2 does not collide with the obstacle.

Therefore, the bi-RRT algorithm is used to find the path point, and the OBB algorithm can determine whether there is a collision between the manipulator joint and the obstacle or between the joints. The pseudo-code for manipulator trajectory planning is as Algorithm 1. The EXTEND function denotes that selects the nearest vertex already in the RRT to the given sample state.[30]

Algorithm 1 Trajectory planning algorithm based on bi-RRT and OBB

Input: x_{init}: initial state; x_{goal}: goal state
Output: Joint angles of manipulator motion $q_i(i = 1, \cdots, 9)$

```
T_a ← x_init, T_b ← x_goal
repeat
    compute joint angles q_i by inverse kinematics;
    Determine whether there is a collision by
        |A'^{i1}_min A'^{i1}_max| + |A'^{i2}_min A'^{i2}_max| < |A'^{i1}_(ia) A'^{i2}_(ia)|_max and
        |A'^{2}_min A'^{2}_max| + |B'^{1}_min B'^{1}_max| < |A'^{2}_(i) B'^{1}_(i)|_max as (1);
    Update T_a and T_b;
    Update x_rand ← RANDOM_STATE();
    Update EXTEND(T_a, x_rand); EXTEND(T_b, x_rand);
until T_a = T_b
```

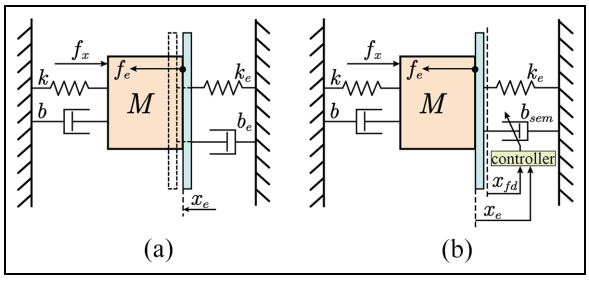

Figure 4. A 1-DOF spring-damping model: (a) physical model of the manipulator end-effector contact with the environment and (b) physical model of the manipulator end-effector contact with the environment based on virtual semi-active damping control.

Improved virtual semi-active damping control algorithm

Considering the contact between the end-effector of the manipulator and the environment, $\boldsymbol{x} \in \mathbb{R}^n$ represents the position and orientation of the end-effector in the workspace, and the dynamic equation of the manipulator in contact with the environment can be written as

$$\boldsymbol{M}_x\ddot{\boldsymbol{x}} + \boldsymbol{C}_x\dot{\boldsymbol{x}} + \boldsymbol{G}_x + \boldsymbol{F}_e = \boldsymbol{F}_x, \tag{2}$$

where $\boldsymbol{M}_x = \boldsymbol{J}^{-T}\boldsymbol{M}(\boldsymbol{q})\boldsymbol{J}^{-1}$, $\boldsymbol{G}_x = \boldsymbol{J}^{-T}\boldsymbol{G}(\boldsymbol{q})$, $\boldsymbol{F}_x = J^{-T}\boldsymbol{\tau}$, $\boldsymbol{C}_x = \boldsymbol{J}^{-T}\big(\boldsymbol{C}(\boldsymbol{q},\dot{\boldsymbol{q}}) - \boldsymbol{M}(\boldsymbol{q})\boldsymbol{J}^{-1}\dot{\boldsymbol{J}}\big)\boldsymbol{J}^{-1}$ denotes the control force; $\boldsymbol{J} \in \mathbb{R}^{n\times n}$ is the Jacobian matrix and $\boldsymbol{F}_e$ is the contact force between the manipulator end-effector and the environment. $\boldsymbol{\tau} \in \mathbb{R}^n$ is the vector of generalized continuous torques acting at the joints; $\boldsymbol{M}(\boldsymbol{q}) \in \mathbb{R}^{n\times n}$ is the mass (inertia) matrix; $\boldsymbol{C}(\boldsymbol{q},\dot{\boldsymbol{q}}) \in \mathbb{R}^{n\times n}$ is the centrifugal-Coriolis matrix and $\boldsymbol{G}(\boldsymbol{q}) \in \mathbb{R}^n$ is the Cartesian gravitational term.

When the manipulator contacts the environment, it can be seen as a spring-damping model, as shown in Figure 4(a), where $\boldsymbol{x}_e$ represents the position of the environment. The depth of the extrusion environment at the manipulator can be written as $\Delta\boldsymbol{x} = \boldsymbol{x} - \boldsymbol{x}_e$, and the contact force can be described as

$$\boldsymbol{F}_e = \boldsymbol{k}_e\Delta\boldsymbol{x} + \boldsymbol{b}_e\Delta\dot{\boldsymbol{x}}, \tag{3}$$

where $\boldsymbol{k}_e, \boldsymbol{b}_e$ represent the stiffness and damping matrix of the environment, respectively. In general, $\boldsymbol{k}_e$ and $\boldsymbol{b}_e$ are usually unknown, which are determined by the dynamic characteristics of the manipulator end-effector and the environment. Since $\boldsymbol{k}_e = \mathrm{diag}\left(k_e^x, k_e^y, k_e^z\right)$ and $\boldsymbol{b}_e = \mathrm{diag}\left(b_e^x, b_e^y, b_e^z\right)$ are symmetric matrices, equation (3) can be written as the contact force of the manipulator along the specified direction

$$f_e = k_e\Delta x + b_e\Delta\dot{x}, \tag{4}$$

where $k_e, b_e \in \mathbb{R}$ denotes the environmental stiffness and damping along the force direction, Δx and $\Delta\dot{x}$ denote the extrusion depth and velocity of the manipulator in the force direction.

When the manipulator does not contact the environment, the manipulator moves according to the command trajectory. When the manipulator contacts the environment, control the posture of the manipulator to maintain a desired contact force $\boldsymbol{F}_d = \mathrm{diag}\left(f_d^x, f_d^y, f_d^z\right)$ with the environment. With a pressure sensor mounted at the end of the manipulator, an effective method to judge the manipulator contacts the environment is the pressure value in each direction feedback by the pressure sensor is zero. However, the pressure sensor can not maintain data at zero due to signal noise even if the manipulator is not in contact with the environment. In this paper, we set a threshold β that can be considered that the manipulator contacts the environment only when $\|\boldsymbol{F}_s\| > \beta$. The threshold β can be denoted as

$$\beta = \lambda_s \max\left(\left\|\boldsymbol{F}_s^{free}\right\|\right), \tag{5}$$

where $\lambda_s > 1$ is the threshold gain coefficient, and $\boldsymbol{F}_s^{free}$ is the feedback value of the pressure sensor during the free movement of the manipulator. Considering[32,33], an improved VSADC is designed as

$$\boldsymbol{F}_c = \begin{cases} \boldsymbol{k}_d(\dot{\boldsymbol{x}} - \dot{\boldsymbol{x}}_d) + \boldsymbol{k}_{p1}(\boldsymbol{x} - \boldsymbol{x}_d) + \boldsymbol{G}_x, \\ \|\boldsymbol{F}_s\| \leqslant \beta \\ \boldsymbol{F}_d + \boldsymbol{k}_{p2}(\boldsymbol{F}_s - \boldsymbol{F}_d) - \mathbf{b}_{sem}(\dot{\boldsymbol{x}} - \dot{\boldsymbol{x}}_e), \\ \|\boldsymbol{F}_s\| > \beta \end{cases} \tag{6}$$

where $\boldsymbol{k}_d = \mathrm{diag}\left(k_d^x, k_d^y, k_d^z\right)$, $\boldsymbol{k}_{p1} = \mathrm{diag}\left(k_{p1}^x, k_{p1}^y, k_{p1}^z\right)$, and $\boldsymbol{k}_{p2} = \mathrm{diag}\left(k_{p2}^x, k_{p2}^y, k_{p2}^z\right)$ are symmetric gain matrices. The position, velocity, and contact force at the end of the manipulator can be obtained by sensors. However, the information related to the environment is hard to be obtained, so $\dot{\boldsymbol{x}}_e$ is defined as the estimated speed of environmental position change.

Then, the virtual semiactive damping $\boldsymbol{b}_{sem} = \mathrm{diag}\left(b^x_{sem}, b^y_{sem}, b^z_{sem}\right)$ can be calculated by

$$\boldsymbol{b}_{sem} = \boldsymbol{b}_f + \boldsymbol{b}_v, \tag{7}$$

where $\boldsymbol{b}_f = \mathrm{diag}\left(b^x_f, b^y_f, b^z_f\right)$ is the defined damping gain, and it represents the energy dissipated in the contact phase. $\boldsymbol{b}_v = \mathrm{diag}\left(b^x_v, b^y_v, b^z_v\right)$ is an active adjustable virtual damping, and $\boldsymbol{b}_v$ in any direction can be calculated as [34]

$$b_v = \min\left[\lambda\left|x - x_{fd}\right|, b_{v\max}\right], \tag{8}$$

where x_{fd} represents the virtual desired position of the manipulator reaching the expected contact force f_d along the direction of the contact force. $\lambda > 0$ is the gain coefficient of the error between the actual position of the manipulator end-effector and the virtual expected position, and $b_{v\max}$ is the saturation value of the given virtual damping. Then, the physical model of virtual semi-active damping control can be shown in Figure 4(b). According to equation (4), it is easy to obtain

$$k_e\left(x_{fd} - x_e\right) + b_e\left(\dot{x}_{fd} - \dot{x}_e\right) = f_d. \tag{9}$$

Due to the position x_e and velocity $\dot{x}_e$ of the environment are unknown, $\hat{x}_e$ and $\dot{\hat{x}}_e$ are assumed as the estimated environmental position and velocity along the movement direction of the manipulator, respectively. Then, from equation (9), it can be obtained that

$$x_{fd} = \frac{f_d - b_e\left(\dot{x}_{fd} - \dot{\hat{x}}_e\right)}{k_e} + \hat{x}_e. \tag{10}$$

Since the impedance coefficient of the environment is unknown, we can assume that the estimated values of the stiffness and damping of the environment are $\hat{k}_e$ and $\hat{b}_e$. Considering equation (4), $\hat{x}_e$ can be expressed as

$$\hat{x}_e = x - \Delta x = x - \frac{f_s - \hat{b}_e\left(\dot{x} - \dot{\hat{x}}_e\right)}{\hat{k}_e}. \tag{11}$$

Assuming that the sampling period of the system is al. Workspace analysis, equation (11) can lead to

$$\hat{x}_e(\varepsilon) = x(\varepsilon) - \frac{f_s(\varepsilon) - \hat{b}_e(\varepsilon)\left[\frac{x(\varepsilon)-x(\varepsilon-1)}{\varepsilon} - \frac{\hat{x}_e(\varepsilon)-\hat{x}_e(\varepsilon-1)}{\varepsilon}\right]}{\hat{k}_e(\varepsilon)}. \tag{12}$$

Then, by recursion, $\hat{x}_e(\varepsilon)$ can be further written as

$$\hat{x}_e(\varepsilon) = x(\varepsilon) - \frac{\varepsilon f_s(\varepsilon) + \hat{b}_e(\varepsilon)\left(x(\varepsilon-1) - \hat{x}_e(\varepsilon-1)\right)}{\varepsilon\hat{k}_e(\varepsilon) + \hat{b}_e(\varepsilon)}. \tag{13}$$

The initial estimated position $\hat{x}^0_e$ can be considered as the position of the manipulator end-effector at the moment of initial contact. Similarly, according to equation (13), we can obtain that

$$x_{fd}(\varepsilon) = \hat{x}_e(\varepsilon) + \frac{\varepsilon f_d(\varepsilon) + \hat{b}_e(\varepsilon)\left(x_{fd}(\varepsilon-1) - \hat{x}_e(\varepsilon-1)\right)}{\varepsilon\hat{k}_e(\varepsilon) + \hat{b}_e(\varepsilon)}. \tag{14}$$

Further, to estimate the impedance parameters $\hat{k}_e$ and $\hat{b}_e$, the following cost function is defined as[32,33]

$$\mathcal{J}(\boldsymbol{z}) = \left(f_s - \hat{k}_e\Delta x - \hat{b}_e\Delta\dot{x}\right)^2, \tag{15}$$

where $\boldsymbol{z} = \left[\hat{k}_e; \hat{b}_e\right]$, $\Delta x = x - \hat{x}_e$, and $\Delta\dot{x} = \dot{x} - \dot{\hat{x}}_e$ represent the depth and velocity of the manipulator penetrating the environment along the force direction, respectively.

PSO is an effective meta-heuristic optimization algorithm, which makes use of the individual sharing of information in the group to produce the evolution from disorder to order in the motion solution space of the whole group, to obtain the optimal solution. Therefore, the cost function (equation (15)) can be used as the fitness value of the PSO algorithm to optimize impedance parameters $\hat{k}_e$ and $\hat{b}_e$. The pseudocode of impedance parameter estimation using PSO is shown in algorithm 2. In general, the learning factor of the PSO in Algorithm 2 can be chosen as $c_1 = c_2 = 2$, and the particle number N can be set as 50.

Simulation and experiment

In our work, the modified Denavit-Hartenberg method and the Lagrange equation are used to establish the kinematic and dynamic model of the manipulator before the simulation and experiments. The gradient projection method[35] is used to solve the inverse kinematics of the manipulator. Due to the limitation of space, it is not covered here. This section presents simulations and experiments about obstacle crossing, and force control to confirm the performance of the designed manipulator and the effectiveness of the theoretical results.

Simulation and experiment of obstacle crossing

To verify the flexibility of the designed modular redundant manipulator, we designed a complex obstacle environment with a size of

Algorithm 2 Environmental impedance parameters and position estimation based on PSO

Input: particle number N, position of the manipulator x, learning factor c_1, c_2, and small value δ
Output: $\mathbf{z}^k, \hat{x}_e^k$
if $f_s \geqslant \beta$ **then**
for $i \leftarrow 1$ to N **do**
initialize velocity $v_i^0 \in \mathbb{R}^2$ and position $\mathbf{z}_i^0 \in \mathbb{R}^2$ for particle i;
evaluate particle i by $\mathcal{J}(\mathbf{z}_i)$ in (15) with $\hat{x}_e^0$ and set the best position of particle i as $\mathbf{p}_{pbesti} = \mathbf{z}_i^0$;
end for
compute the global best position $\mathbf{p}_{gbest} = \text{find}\left(\mathbf{z}_i^0, \min\left\{\mathbf{p}_{pbesti}\right\}\right)$
While $\mathcal{J}(z) > \delta$ **do**
For $i \leftarrow 1$ to N **do**
$r_1 = \text{rand}(0, 1); r_2 = \text{rand}(0, 1)$
$v_i^{k+1} = v_i^k + c_1 r_1 \left(\mathbf{p}_{pbesti} - \mathbf{z}_i^k\right) + c_2 r_2 \left(\mathbf{p}_{gbest} - \mathbf{z}_i^k\right)$
$\mathbf{z}_i^{k+1} = \mathbf{z}_i^k + v_i^k$
Compute $\hat{x}_e^k$ by (25) and $\mathcal{J}(\mathbf{z}_i^k)$ by (27)
if $\mathcal{J}(\mathbf{z}_i^{k+1}) < \mathcal{J}\left(\mathbf{p}_{pbesti}\right)$ **then**
$\mathbf{p}_{pbesti} \leftarrow \mathbf{z}_i^{k+1}$
end if
if $\mathcal{J}\left(\mathbf{p}_{pbesti}\right) < \mathcal{J}\left(\mathbf{p}_{gbesti}\right)$ **then**
$\mathbf{p}_{gbesti} \leftarrow \mathbf{p}_{pbesti}$
end if
end for
end while
end if

600 mm × 530 mm × 1000 mm, mainly including the narrow space of three baffles, as shown in Figure 5(a) and (b). The redundant manipulator was required to enter the obstacle along the direction m and cross the obstacle along the direction n. The initial joint angles was set as [0°, 0°, 0°, 0°, 0°, 0°, 0°, 0°, 80°], and the target pose was given as [517.6 mm, 1060.3 mm, −3.3 mm, 91.3°, −3.8°, −9.5°]. The time of the manipulator crossing the obstacle was assumed as 40 s, and the angles of each joint were recorded in each 5 s. Then, the changing process of each joint of the manipulator obtained by simulation is shown in Figure 5(c).

To illustrate the superiority of the designed algorithm, the traditional RRT is used to replace the bi-RRT algorithm in this paper for five times of obstacle crossing simulation. The time comparison data are obtained by randomly running the algorithm under the same conditions. The personal computer has an Intel(R) Core (TM) i7-7700 central processing unit running at 3.60 GHz with 8.00 GB RAM, and the software is MATLAB R2017b. The simulation results in Figure 5(d) show that the performance of the proposed algorithm has an obvious advantage in terms of calculation time.

Further, the process of the manipulator crossing the obstacle environment is simulated by ADAMS, as shown in Figure 5(e). The joint angles of each stage obtained by simulation are sent to the controller so that the manipulator passes through the set obstacle environment. From Figure 5(f), it can be seen that the designed manipulator can flexibly cross the complex and narrow obstacle environment, and there is no collision with obstacles in the experimental process (Supplemental Movie 1). The path of the manipulator joint crossing the obstacle environment is almost consistent with the path obtained by simulation. The joint angle of the manipulator collected in the experiment is shown in Figure 5(g), and it can be seen that the actual motion of the manipulator is consistent with the change of the joint angle obtained by simulation in Figure 5(c). Compared with the traditional manipulator, the designed redundant manipulator combined with the designed obstacle avoidance algorithm has high flexibility and can perform tasks in complex obstacle environments.

Force control experiment

To illustrate the effectiveness of the proposed force control algorithm in the contact force control of the redundant manipulator, a relevant force control experiment was performed. A balloon was fixed at the end of the UR10 robot, and the position of the balloon and the impedance parameters are unknown. As shown in Figure 6(a), the end of the UR robot moved 10 cm to the left at the speed of 0.01 m/s and then moved 20 cm to the right at the same speed (Supplemental Movie 2). A pressure sensor (OptoForce HEX-70-XE-200N with a force acquisition period of 0.01 s) was installed at the end of the redundant manipulator. Only the pressure control of the manipulator in a single direction was considered, and the desired pressure was set to 10 N.

In this experiment, the threshold gain coefficient λ_s was set as 1.4, and control parameters were set as $b_f = 50$, $\lambda = 1000$, $\delta = 0.1$, and $\mathbf{z}_0 = [500]^T$, respectively. From Figure 6(b), it can be seen that the contact force at the end of the redundant manipulator has three obvious chattering after reaching 10 N, which is due to the sudden stop and start of the UR robot. The manipulator end-effector begins to contact the balloon at 7.5 s, and the contact pressure is stable at 10 N at 11.8 s. It can be seen from Figure 6(c) to (e) that the impedance parameters and position of the environment can be estimated during the contact process of the manipulator with the balloon. Although the impedance parameters are not actual, the controller can still obtain a good force control performance. As a result, combined with the improved VSADC algorithm, the redundant manipulator can have good interaction ability with the unknown environment and can be used to perform complex interactive tasks.

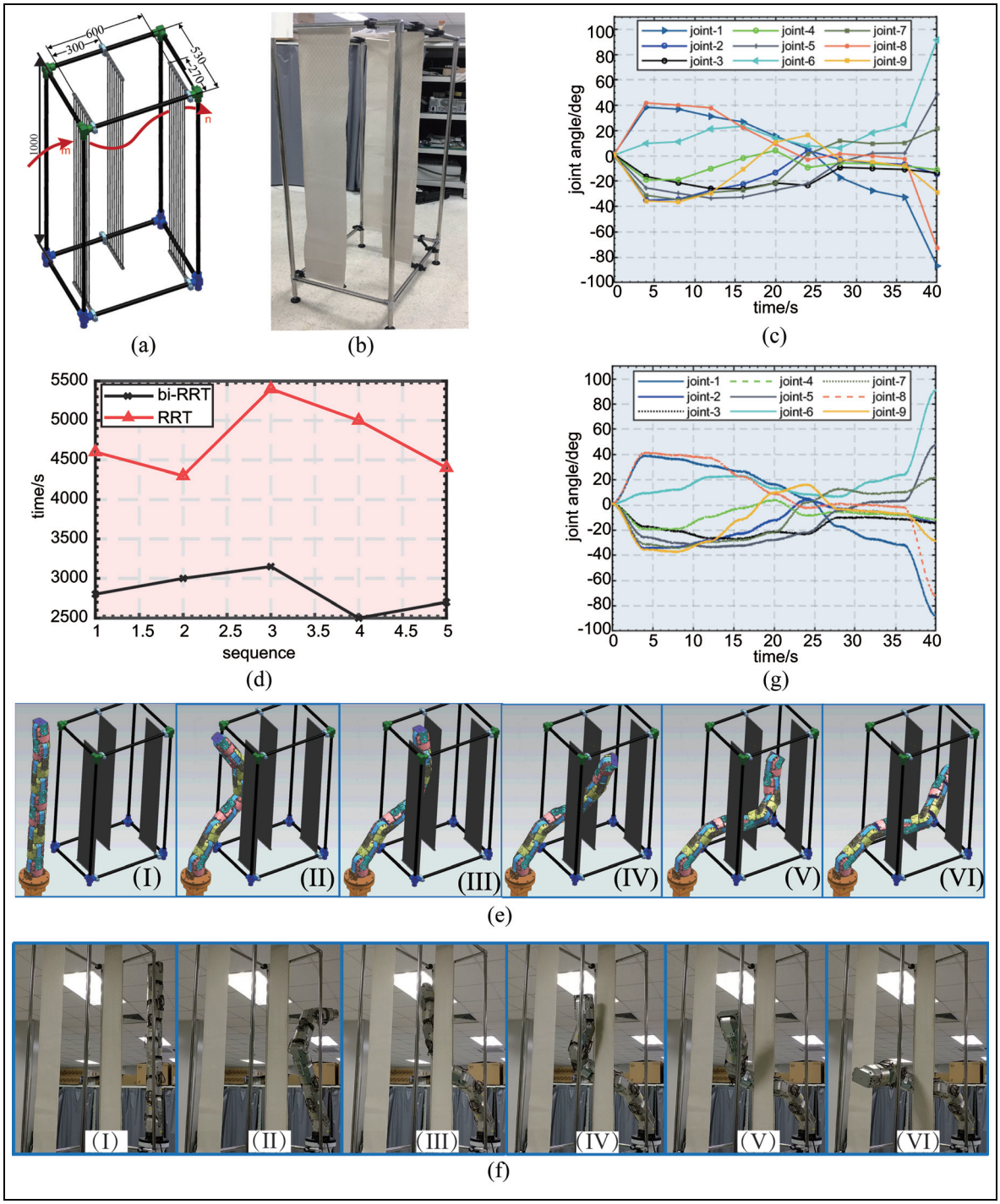

Figure 5. Obstacle crossing experiment of the redundant manipulator: (a) obstacle model, (b) obstacle object, (c) change of each joint angle of the manipulator with time obtained by simulation, (d) time required by traditional RRT algorithm and bi-RRT algorithm in trajectory planning, (e) simulation process of the manipulator crossing obstacle, (f) experimental process of the manipulator crossing obstacle, and (g) joint curves of the manipulator crossing obstacle in the experiment.

Discussion and future work

Since rigid modular redundant manipulators have significant advantages in flexibility and are different from soft manipulators, they have higher control accuracy and force control ability. Therefore, the designed redundant manipulator may play an important role in the on-orbit construction of large space telescopes to perform the handling, assembly, detection, and other tasks. Undoubtedly, these tasks are a great challenge to the obstacle avoidance ability of the manipulator and the interaction ability of the unstructured environment. Two control algorithms proposed for redundant manipulators in this paper show two measures to address this challenge.

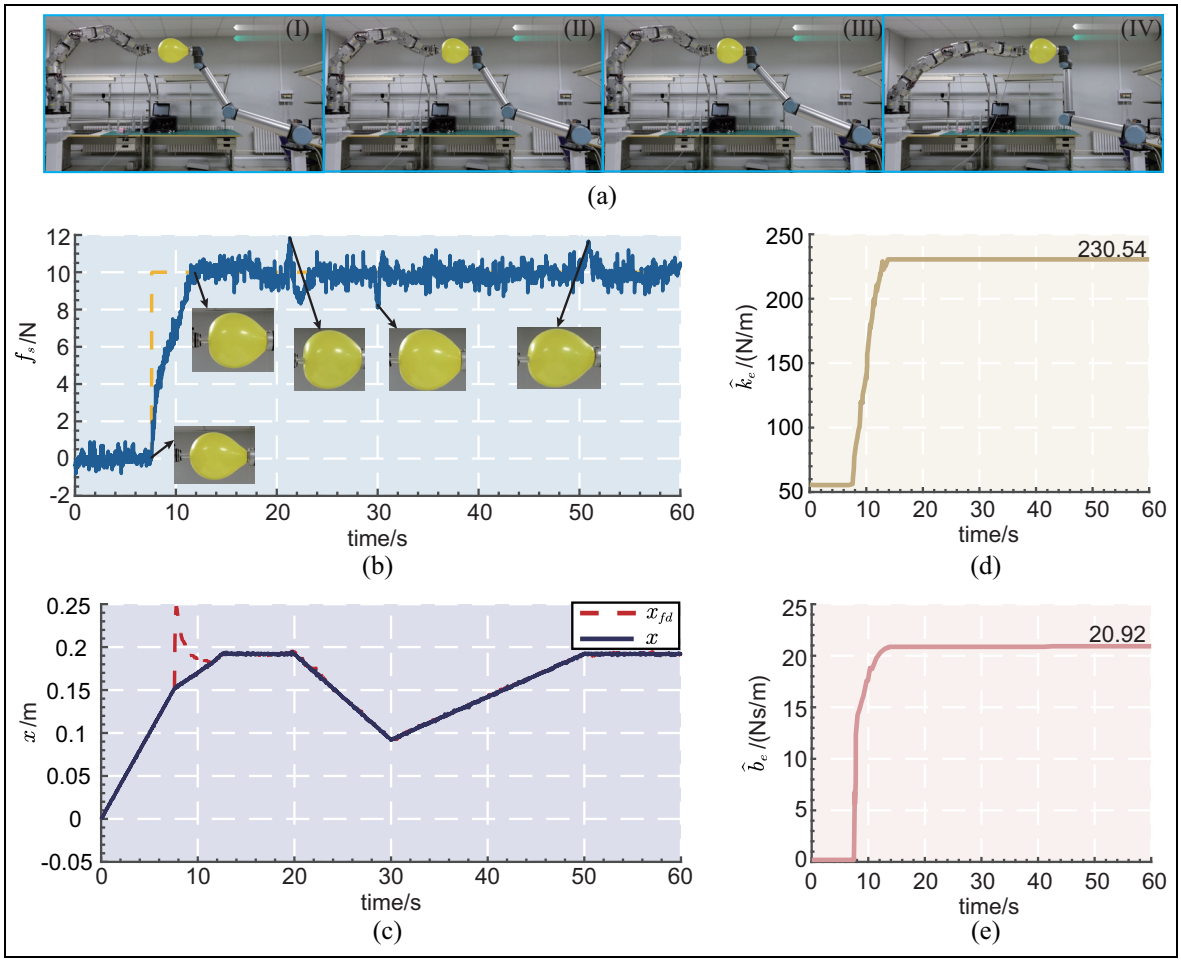

Figure 6. Force control experiment of the redundant manipulator: (a) the force control experiment process of the manipulator, (b) contact force between the manipulator end-effector and the balloon, (c) the actual position and the virtual desired position of the manipulator end-effector, (d) the estimated impedance parameter $\hat{k}_e$, and (e) the estimated impedance parameter $\hat{b}_e$.

The proposed obstacle avoidance control algorithm can be used in complex obstacle environments and has high computational efficiency. Different from the most existing trajectory planning algorithms[17,18,36,37] for redundant manipulators, a more complex 3D space obstacle is set in this paper, and not only physical stimulation but also corresponding experiments are carried out. It is worth noting that this work assumes that the obstacle is completely known and the obstacle is static. However, for the actual working environment, the position and shape of the obstacle are not readily available and may be dynamic. In future work, some speed space algorithms, such as the dynamic-window algorithm,[38] will be considered for obstacle avoidance in redundant manipulators.

In our work, we have demonstrated the interaction between the redundant manipulator and the unknown environment and the rapid estimation of the environmental state. In some existing work,[32,33] impedance controllers for manipulators only can be applied to static environments, and the prior knowledge about the environmental position was assumed to be known.[39,40] The proposed improved virtual semi-active damping control algorithm can be used not only for static environments but also for force interaction in unknown dynamic environments. Meanwhile, the possible influence of measurement noise on the control performance was considered, which has important practical application. It is worth mentioning that the PSO may fall into local optimal when searching for optimal impedance parameters. Fortunately, some advanced optimization algorithms, such as the group search optimizer algorithm,[41] provide us with valuable ideas for optimizing impedance parameters in the future.

Besides the two control algorithms described in this paper, the modular design scheme is adopted for our designed manipulator, even if it is not emphasized too much in this paper. Compared with traditional manipulators, modular joints can benefit versatility, robustness, and low-cost manufacturing. In particular, different numbers of joints can be assembled into the manipulator depending on the task requirements, and broken joints can be easily replaced.

Conclusion

This paper focuses on a novel 9-DOF modular redundant manipulator composed of nine identical modular

joints in series. The compact structure design and two-stage deceleration make the joint keep a small volume and large output torque. We demonstrated a trajectory planning algorithm based on the bi-RRT and OBB, which is used to plan a reasonable trajectory for the redundant manipulator to avoid collision with obstacles. The simulation and experiment of crossing obstacles for the redundant manipulator were implemented in a complex 3D obstacle environment. Meanwhile, we have demonstrated an improved VSADC algorithm. The experimental results show that even without prior knowledge of the environment, the manipulator can maintain the desired contact force with the dynamic environment. Therefore, the designed redundant manipulator is expected to be applied in complex and narrow environments for interaction tasks in the future.

Declaration of conflicting interests

The author(s) declared no potential conflicts of interest with respect to the research, authorship, and/or publication of this article.

Funding

The author(s) disclosed receipt of the following financial support for the research, authorship, and/or publication of this article: This work was supported by the National Natural Science Foundation of China Under Grant No.11972343.

Supplemental material

Supplemental material for this article is available online.

References

1. Mu Z, Liu T, Xu W, et al. Dynamic feedforward control of spatial cable-driven hyper-redundant manipulators for on-orbitservicing. *Robotica* 2019; 37(1): 18–38.
2. Buckingham R and Graham AE. Nuclear snake-arm robots. *Ind Rob Int J* 2012; 39(1): 6–11.
3. Su H, Sandoval J, Vieyres P, et al. Safety-enhanced collaborative framework for tele-operated minimally invasive surgery using a 7-dof torque-controlled robot. *Int J Control Autom Syst* 2018; 16(6): 2915–2923.
4. Anderson VC. Tensor arm manipulator design. *Trans ASME* 1967; 67: 1–12.
5. Ju R, Zhang D, Xu J, et al. Design, modeling, and kinematics analysis of a modular cable-driven manipulator. *J Mech Rob* 2022; 14(6): 064501.
6. Tao J, Qin C, Xiong Z, et al. Optimization and control of cable tensions for hyper-redundant snake-arm robots. *Int J Control Autom Syst* 2021; 19(11): 3764–3775.
7. Guardiani P, Ludovico D, Pistone A, et al. Design and analysis of a fully actuated cable-driven joint for hyper-redundant robots with optimal cable routing. *J Mech Rob* 2022; 14(2): 1–13.
8. Saab W, Rone WS, Kumar A, et al. Design and integration of a novel spatial articulated robotic tail. *IEEE-ASME Trans Mechatron* 2019; 24(2): 434–446.
9. Wright C, Buchan A, Brown B, et al. Design and architecture of the unified modular snake robot. In: *2012 IEEE international conference on robotics and automation*, Saint Paul, MN, 14–18 May 2012, pp. 4347–4354. New York, NY: IEEE.
10. Wright C, Johnson A, Peck A, et al. Design of a modular snake robot. In: *2007 IEEE/RSJ international conference on intelligent robots and systems*, San Diego, CA, 29 October–2 November 2007, pp. 2609–2614. New York, NY: IEEE.
11. Mu Z, Wang H, Xu W, et al. Two types of snake-like robots for complex environment exploration: design, development, and experiment. *Adv Mech Eng* 2017; 9(9): 1–15. Doi: 10.1177/1687814017721854.
12. Gallardo J, Orozco H, Rico JM, et al. A new spatial hyper-redundant manipulator. *Rob Comput Integr Manuf* 2009; 25(4): 703–708.
13. Zhao Y, Jin L, Zhang P, et al. Inverse displacement analysis of a hyper-redundant elephant's trunk robot. *J Bionic Eng* 2018; 15(2): 397–407.
14. Zhao Y, Song X, Zhang X, et al. A hyper-redundant elephant's trunk robot with an open structure: design, kinematics, control and prototype. *Chin J Mech Eng* 2020; 33(1): 1–19.
15. Hu B, Cui H, Shi D, et al. Reachable workspace determination for a spatial hyper-redundant manipulator formed by several parallel manipulators. *J Mech Sci Technol* 2019; 33(2): 869–877.
16. Brown H, Schwerin M, Shammas E, et al. Design and control of a second-generation hyper-redundant mechanism. In: *2007 IEEE/RSJ international conference on intelligent robots and systems*, San Diego, CA, 29 October–2 November 2007, pp. 2603–2608. New York, NY: IEEE.
17. Safeea M, Bèarèe R and Neto P. Collision avoidance of redundant robotic manipulators using newton's method. *J Intell Rob Syst* 2020; 99(3): 673–681.
18. Wang W, Zhu M, Wang X, et al. An improved artificial potential field method of trajectory planning and obstacle avoidance for redundant manipulators. *Int J Adv Rob Syst* 2018; 15(5): DOI: 10.1177/1729881418799562.
19. Mu Z, Xu W and Liang B. Avoidance of multiple moving obstacles during active debris removal using a redundant space manipulator. *Int J Control Autom Syst* 2017; 15(2): 815–826.
20. Zhang H, Jin H, Liu Z, et al. Real-time kinematic control for redundant manipulators in a time-varying environment: multiple-dynamic obstacle avoidance and fast tracking of a moving object. *IEEE Trans Industr Inform* 2019; 16(1): 28–41.
21. Izadbakhsh A and Khorashadizadeh S. Robust impedance control of robot manipulators using differential equations as universal approximator. *Int J Control* 2018; 91(10): 2170–2186.
22. Diolaiti N, Melchiorri C and Stramigioli S. Contact impedance estimation for robotic systems. *IEEE-ASME Trans Mechatron* 2005; 10(2): 925–935.
23. Ma J, Dong S, Chen G, et al. A data-driven normal contact force model based on artificial neural network for complex contacting surfaces. *Mech Syst Signal Process* 2021; 156: 107612.
24. Fernando H, Marshall JA and Larsson J. Iterative learning-based admittance control for autonomous excavation. *J Intell Rob Syst* 2019; 96(3): 493–500.

25. Wang R, Zhang X and Fang Y. Visual tracking of mobile robots with both velocity and acceleration saturation constraints. *Mech Syst Signal Process* 2021; 150: 107274.
26. Zhao Z, He S, Zhao Y, et al. Workspace analysis for a 9-DOF hyper-redundant manipulator based on an improved monte Carlo method and voxel algorithm. In: *2018 IEEE international conference on mechatronics and automation (ICMA)*, Changchun, China, 5–8 August 2018. New York, NY: IEEE.
27. Taherifar A, Salarieh H and Alasty A. Kinematic control of a new hyper-redundant manipulator with lockable joints. *Sci Iran* 2013; 20(6): 1742–1752.
28. Xu X, Ananthanarayanan H and Ordonez R. Design and construction of 9-DOF hyper-redundant robotic arm. In: *NAECON 2014 -IEEE national aerospace and electronics conference*, Dayton, OH, 24–27 June 2014, pp. 321–326. New York, NY: IEEE.
29. LaValle SM and Kuffner JJ. *Rapidly-exploring random trees: progress and prospects. Steven M. Lavalle, Iowa State University, A James J. Kuffner, Jr., University of Tokyo, Tokyo, Japan*. Boca Raton, FL: CRC Press, 2001, pp.303–307.
30. LaValle SM and Kuffner JJ. Randomized kinodynamic planning. *Int J Rob Res* 2001; 20(5): 378–400.
31. Akenine-Moller T, Moller T and Haines E. *Real-time rendering*. Boca Raton, FL: CRC Press, 1997.
32. Wang W, Li A, Li Q, et al. Virtual semi-active damping learning control for robot manipulators interacting with unknown environment. *J Vib Control* 2021; 27(23–24): 2807–2818.
33. Wang W, Li Q, Lu C, et al. Impedance estimation for robot contact with uncalibrated environments. *Mech Syst Signal Process* 2021; 159: 107819.
34. Stegall P, Zanotto D and Agrawal SK. Variable damping force tunnel for gait training using alex iii. *IEEE Robot Automat Lett* 2017; 2: 1495–1501.
35. Liegeois A. Automatic supervisory control of the configuration and behavior of multi-body mechanisms. *IEEE Trans Syst Man Cybern* 1977; 7(12): 868.
36. Lafmejani AS, Doroudchi A, Farivarnejad H, et al. Kinematic modeling and trajectory tracking control of an octopus-inspired hyper-redundant robot. *IEEE Robot Automat Lett* 2020; 5: 3460–3467.
37. Ananthanarayanan H and Ordóñez R. A fast converging optimal technique applied to path planning of hyper-redundant manipulators. *Mech Mach Theory* 2017; 118: 231–246.
38. Ozdemir A and Sezer V. A hybrid obstacle avoidance method: follow the gap with dynamic window approach. In: *2017 first IEEE international conference on robotic computing (IRC)*, Taichung, Taiwan, 10–12 April 2017, pp. 257–262. New York, NY: IEEE.
39. Duan J, Gan Y, Chen M, et al. Adaptive variable impedance control for dynamic contact force tracking in uncertain environment. *Rob Auton Syst* 2018; 102: 54–65.
40. Cao H, Chen X, He Y, et al. Dynamic adaptive hybrid impedance control for dynamic contact force tracking in uncertain environments. *IEEE Access* 2019; 7: 83162–83174.
41. Abualigah LM. Group search optimizer: a nature-inspired meta-heuristic optimization algorithm with its results, variants, and applications. *Neural Comput Appl* 2021; 33(7): 2949–2972.